Grid Synchronization Control for Grid-connected Voltage Source Converters Based on Voltage Dynamics of DC-link Capacitor

Chunyi Han, *Student Member*, *IEEE*, Lei Shang, *Senior Member*, *IEEE*, Shi Su, Xuzhu Dong, *Senior Member*, *IEEE*, Bo Wang, *Senior Member*, *IEEE*, Hao Bai, *Member*, *IEEE*, and Wei Li, *Member*, *IEEE*

***Abstract*—This paper proposes a grid synchronization control strategy for the grid-connected voltage source converters (VSCs) based on the voltage dynamics of the DC-link capacitor in the VSC. The voltage dynamics of the DC-link capacitor are used to regulate the frequency and phase angle of the inner potential of the VSC, synchronizing the VSC with grid. Firstly, in the proposed strategy, the active power regulation and grid synchronization of the VSC are combined, which are separated in the traditional control strategy. This can avoid the instability of the VSC in a weak grid with a low short circuit ratio (SCR), aroused by the dynamic interaction between the separated control loops in traditional control strategies. Secondly, the energy stored in the DC-link capacitor is directly coupled with the grid via the inner potential of the VSC, and the inertia characteristic is naturally featured in the inner potential by the proposed strategy. With the increase of the capacitance, the natural inertial response of the VSC is helpful to improve the grid frequency dynamic. Finally, simulation results are presented to validate the correctness and effectiveness of the proposed strategy on the enhancement of the grid frequency and voltage dynamic support capability.**

***Index Terms*—DC-link voltage dynamics, grid synchronization control, grid frequency and voltage dynamic support, small-signal stability, weak grid.**

I. Introduction

RECENTLY, the solar power generations [1], [2], wind power generations [3], [4], voltage source converter based high-voltage direct current (VSC-HVDC) [5], static synchronous compensator (STATCOM) [6], and energy storage [7], [8] have been rapidly developed and become the important component of power systems. The grid-connected voltage source converters (VSCs) are the interfaces of wind power generations, solar power generations, VSC-HVDC, STACOM, energy storage, etc. with grids, which directly affect the dynamic performance of these facilities. Thus, the dynamic behavior of VSCs has won more attention of researchers, engineers, etc.

Typical grid-connected VSCs are controlled by multi-series and parallel control loops [9], e.g., DC voltage control [10]-[13], phase locked loop (PLL) [14], [15], AC current control, and reactive power control. There are many studies on improving the dynamic performance of the VSCs on the power transfer and DC voltage regulation [10]-[13]. In the traditional control structure, the PLL is used to synchronize the VSC with the grid [14], [15] and the DC voltage control is designed to maintain the DC-link voltage constant to transfer the power injected into the DC link from other power sources. Under normal grid conditions with a high short circuit ratio (SCR) (≥ 2), the VSC based on traditional control can work well to precisely regulate the power of the VSC exchanged with the grid. However, some instability phenomena have been published, when the traditional-control-based VSC is connected to the weak grid with a low SCR (≤ 2) [16]-[20]. Some studies suggest that the oscillation instability is aroused by the dynamic interactions between different control loops of the traditional controls in the VSC, e.g., the PLL control and DC voltage control [21]. Thus, the grid synchronization and power regulation are combined to avoid the instability aroused by the interactions, which is one of the most important purposes to modify the control of the VSC in this paper.

Moreover, with the increasing penetrance of the VSC-based facilities, the impact of the VSC on grid frequency and voltage has received more attention. On the one side, the supplementary signals are added in the power regulations of the VSC for dynamic frequency and voltage support [22]-[26]. In [27], stiffness compensation provides the theoretical foundation for dynamic voltage analysis and improves the control strategy for the VSC to emulate the dynamic frequency and voltage support response of traditional synchronous

Manuscript received: November 8, 2022; revised: March 9, 2023; accepted: August 17, 2023. Date of CrossCheck: August 17, 2023. Date of online publication: September 22, 2023.

This work was supported by Science and Technology Project of Yunnan Power Grid Co., Ltd. (No. YNKJXM20222105).

C. Han, L. Shang (corresponding author), X. Dong, and B. Wang are with Hubei Engineering and Technology Research Center for AC/DC Intelligent Distribution Network, School of Electrical Engineering and Automation, Wuhan University, Wuhan 430072, China (e-mail: hanchunyi@whu.edu.cn; shanglei@whu.edu.cn; dongxz@whu.edu.cn; whwdwb@whu.edu.cn).

S. Shi is with the Electric Power Research Institute, Yunnan Power Gird Co., Ltd., Kunming 650217, China (e-mail: 472732908@qq.com).

H. Bai and W. Li are with China Southern Power Grid Electric Power Research Institute, China Southern Power Grid Co., Ltd., Guangzhou 510000, China (e-mail: baihao@csg.cn; liwei2732@126.com).

DOI: 10.35833/MPCE.2022.000738

generators (SGs). In [28]-[30], all the mechanical and electrical equations are conducted in the VSC to drive the VSC to emulate the dynamic behavior of SGs. In [31], the virtual synchronous control is used in the doubly-fed induction generator (DFIG) for more stable operation in weak grid and dynamic frequency support of the DFIG-based wind turbine. In [32]-[34], the power synchronization control is presented to enhance the stability of the VSC-HVDC to promote active power transmission when connected into the weak grid. However, direct DC voltage regulation is still not involved in these studies. Thus additional control loops are necessary to regulate the DC voltage directly. In [35], a novel control method is proposed by utilizing the voltage dynamics of the DC-link capacitor to realize self-synchronization. Based on [35], in [36], the control strategy of DC voltage droop control is proposed, which makes all the VSC stations involved in DC voltage regulation and power sharing, and the multi-terminal system presents better stability and dynamic performance. But the inner current control still exists and the dynamic support capability for the grid frequency and voltage of the VSC is not yet concerned.

This paper proposes a grid synchronization control strategy for the grid-connected VSC to directly synchronize the output voltage (i.e., inner potential) of the VSC with the grid based on the voltage dynamics of the DC-link capacitor in the VSC, which combines the grid synchronization and the active power regulation. Moreover, the dynamic support capability for grid frequency and voltage is featured in the VSC by the proposed control strategy.

The rest of this paper is organized as follows. Section II presents the traditional control structure of VSCs and the instability phenomenon in weak grids. Then, the principle of the proposed strategy and its application in VSCs are presented in Section III. Moreover, the control design and stability of the proposed strategy in weak grids are analyzed in Section IV. Furthermore, the dynamic frequency and voltage support capability of the VSC based on the proposed strategy is simulated and discussed in Section V. Finally, the conclusions are drawn in Section VI.

II. Traditional Control Structure of VSCs and Instability Phenomenon in Weak Grids

A. VSC Model

The typical topology structure of grid-connected VSCs is shown in Fig. 1. The power source is injected into the DC-link capacitor, e. g., wind power, solar power, and energy storage. A chopper is on the DC side to balance the power. The AC side of the VSC is connected to the grid through the filter.

On the AC side, the relationship between the output voltage and current of the VSC can be expressed as:

$$\boldsymbol{I}=\frac{\boldsymbol{U}_c-\boldsymbol{U}_t}{\mathrm{j}X_c} \tag{1}$$

where $\boldsymbol{U}_c$ and $\boldsymbol{U}_t$ are the equivalent potential vectors of the output voltage of the VSC by pulse width modulation (PWM) and the terminal voltage of the VSC, respectively; $\boldsymbol{I}$ is the output current of the VSC; and X_c is the impedance of the filter of the VSC.

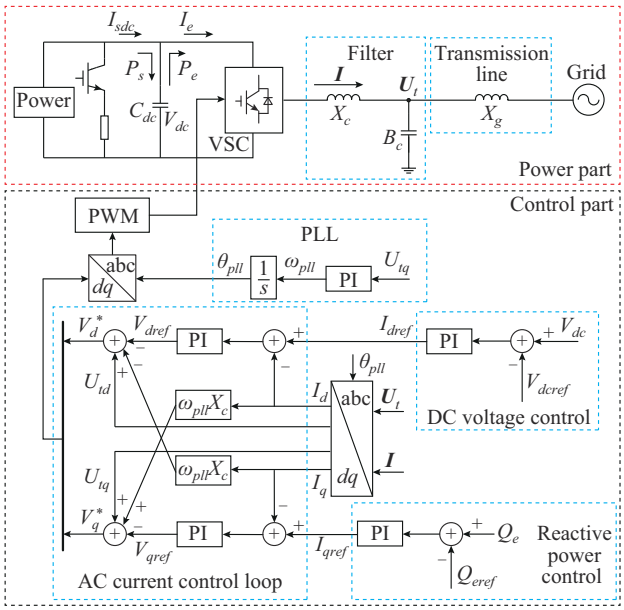

Fig. 1. Typical topology structure of grid-connected VSCs.

The instantaneous active and reactive power outputs P_e and Q_e of the VSC can be calculated by:

$$\begin{cases} P_e = U_{td}I_d + U_{tq}I_q \\ Q_e = -U_{td}I_q + U_{tq}I_d \end{cases} \tag{2}$$

where U_{td} and U_{tq} are the d-axis and q-axis components of the terminal voltage of the VSC, respectively; and I_d and I_q are the d-axis and q-axis components of the output current of the VSC, respectively.

On the DC-link side, the DC voltage of the DC-link capacitor is related to the injected and output active power of the VSC, which can be expressed as:

$$\frac{1}{2}C_{dc}V_{dc}^2 = \int \left(P_s - P_e\right)\mathrm{d}t \tag{3}$$

where P_s is the active power injected from the power source, e.g., wind power, solar power, and energy storage; V_{dc} is the DC-link voltage; and C_{dc} is the capacitor connected to the DC link of the VSC.

Ignoring the loss of the VSC, the output active power of the DC capacitor is equal to the output active power of the VSC, i. e., P_e. The active power injected into the DC link can be expressed as:

$$P_s = V_{dc}I_{sdc} \tag{4}$$

where I_{sdc} is the current injected into the DC capacitor from the power source in the preceding stage.

B. Traditional Control Strategy of Grid-connected VSCs

Typically, the traditional control strategy of grid-connected VSCs includes AC current control, DC voltage control, and PLL control. In grid-connected VSCs, the injected AC current is regulated for the active and reactive power exchang-

ing with grids and the DC voltage control is used to maintain DC voltage for transferring the power injected into the DC link from other power sources. Moreover, the reactive power of the VSC is regulated via the reactive power control. Furthermore, a PLL is employed to synchronize the VSC with grid.

The AC current control aims to regulate the current injected into the grid from the AC side of the VSC according to the current reference of the DC voltage control. Generally, the AC current control is implemented in the synchronous rotating reference based on the PLL. Typical current control is designed as:

$$\begin{cases} V_d^* = U_{td} - V_{dref} - \omega_{pll} X_c I_q \\ V_q^* = U_{tq} - V_{qref} + \omega_{pll} X_c I_d \end{cases} \tag{5}$$

where V_d^* and V_q^* are the d-axis and q-axis components of the output voltage reference of the VSC, respectively; ω_{pll} is the angular frequency output by the PLL; and V_{dref} and V_{qref} are the d-axis and q-axis components of the output voltage reference of the proportional-integral (PI) controller, respectively.

The PI controller in the AC current control of the VSC is usually designed as:

$$\begin{cases} V_{dref} = K_{pc}\left(I_{dref} - I_d\right) + K_{ic}\int\left(I_{dref} - I_d\right)\mathrm{d}t \\ V_{qref} = K_{pc}\left(I_{qref} - I_q\right) + K_{ic}\int\left(I_{qref} - I_q\right)\mathrm{d}t \end{cases} \tag{6}$$

where K_{pc} and K_{ic} are the proportional and integral control parameters of the AC current controller, respectively; and I_{dref} and I_{qref} are the d-axis and q-axis components of the output current reference of the VSC, respectively.

The DC voltage control is designed to maintain the DC-link voltage by setting the d-axis current reference of the VSC.

$$I_{dref} = K_{pdc}\left(V_{dc} - V_{dcref}\right) + K_{idc}\int\left(V_{dc} - V_{dcref}\right)\mathrm{d}t \tag{7}$$

where K_{pdc} and K_{idc} are the proportional and integral control parameters of the DC voltage control, respectively; and V_{dcref} is the DC-link voltage reference of the VSC.

The reactive power control is designed to regulate the reactive power of the VSC by setting the q-axis current reference of the VSC.

$$I_{qref} = K_{pr}\left(Q_{eref} - Q_e\right) + K_{ir}\int\left(Q_{eref} - Q_e\right)\mathrm{d}t \tag{8}$$

where K_{pr} and K_{ir} are the proportional and integral control parameters of the reactive power control, respectively; and Q_{eref} is the instantaneous reactive power reference of the VSC.

The PLL control is usually designed as:

$$\begin{cases} \omega_{pll} = K_{ppll} U_{tq} + K_{ipll}\int U_{tq}\mathrm{d}t \\ \theta_{pll} = \omega_0 \int \omega_{pll}\mathrm{d}t \end{cases} \tag{9}$$

where ω_0 is the synchronous speed; K_{ppll} and K_{ipll} are the proportional and integral control parameters of the PLL, respectively; and θ_{pll} is the power angle of the PLL.

C. Instability Phenomenon of VSC Connected into Weak Grid Based on Traditional Control Strategy

The traditional control strategy is able to regulate the output active power of the VSC under the normal operation condition with the SCR equal to 2.5, as shown in Fig. 2. But when the VSC is connected to the weak grid with a low SCR (equal to 1.3), some instability phenomenon may occur [16], [18]. As shown in Fig. 2, the oscillation instability phenomenon can be observed when the SCR changes from 2.5 to 1.3. In the weak grid, the output active and reactive power of the VSC affects the terminal voltage, and the PLL synchronizes with the grid based on the phase of the terminal voltage. In [19] and [21], detailed analysis has been deeply discussed and it is believed that the complicated dynamic interactions are the main reason for the oscillation instability of the VSC [21] between the control loops of the traditional control strategies, e.g., the PLL control, DC-voltage control, and reactive power control.

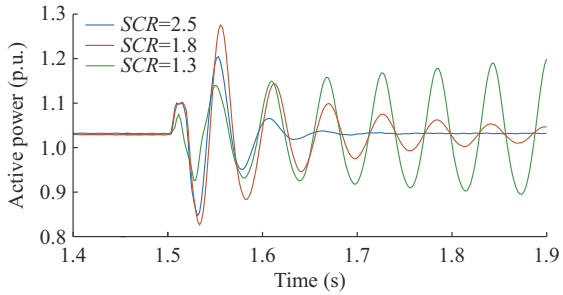

Fig. 2. Active power response of VSC based on traditional control strategy with different SCRs.

To sum up, from the perspective of the power system, the partial drawbacks of the traditional VSC focused on by this paper are summarized as follows.

1) The dynamic active and reactive power support capability of the VSC is weak due to the joint effect of the PLL and cascaded inner current control loops [37].

2) The instability in weak grids may be aroused by the interaction between the PLL and the DC voltage control [18]-[21].

III. Principle of Proposed Strategy and Its Application in VSCs

PLL is mostly used to synchronize a VSC with the power grid in the traditional control structure. The oscillation instability is partly aroused due to the interaction between the PLL and DC voltage control loops in a weak grid, and the traditional control lacks the ability of inertia support. This section proposes a control strategy by combining the grid synchronization and power regulation of the VSC called the DC voltage synchronization control (DCVSynC), which can effectively avoid the dynamic interaction between different control loops and improve the dynamic response of frequency and voltage by providing power support.

A. Synchronization Mechanism

Synchronization is the coordination of events to operate a

system in unison. In power systems, synchronization means all the power generators are rotating at the same speed and keep the power angles constant relative to the rotating speed of the grid ω_g. For an SG, the swing motion equation is used to describe the synchronization of the SG with the power grid, as shown in Fig. 3(a) and (10).

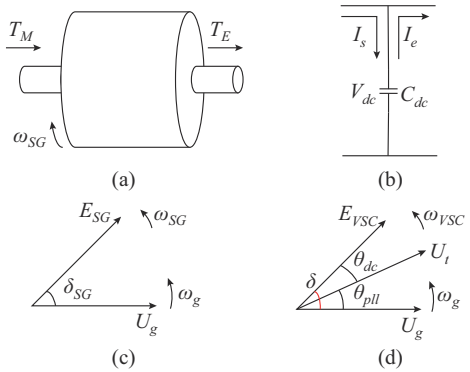

Fig. 3. Energy and power transmission of SG and DC capacitor of VSC and power transfer and grid synchronization of SG and typical VSC. (a) Energy and power transmission of SG. (b) Energy and power transmission of DC capacitor. (c) Power transfer and grid synchronization of SG. (d) Power transfer and grid synchronization of typical VSC.

$$\begin{cases} J\dfrac{\mathrm{d}\omega_{SG}}{\mathrm{d}t} = T_M - T_E - T_D = \dfrac{P_M}{\omega_{SG}} - \dfrac{P_E}{\omega_{SG}} - \dfrac{P_D}{\omega_{SG}} \\ \dfrac{\mathrm{d}\delta_{SG}}{\mathrm{d}t} = \omega_0\omega_{SG} \end{cases} \tag{10}$$

where J and ω_{SG} are the rotor inertia constant and rotating speed of the SG, respectively; δ_{SG} is the power angle of the SG; T_M, T_E, and T_D are the mechanical, electromagnetic, and damping torques of the SG, respectively; and P_M, P_E, and P_D are the input mechanical, output electromagnetic, and damping power of the SG, respectively.

The output electromagnetic power of the SG is expressed as:

$$P_E = \frac{E_{SG}U_g}{X_s}\sin\delta_{SG} \tag{11}$$

where E_{SG} and U_g are the inner potential of the SG and grid voltage, respectively; and X_s is the equivalent impedance of the SG.

For the SG, the input mechanical and output electromagnetic torques drive the rotor in synchronization with grid. When the rotating speed of the SG is higher than the grid frequency, the power angle is enlarged and then the electromagnetic torque increases to reduce the rotating speed of the SG to pull the SG into synchronization. This is an important characteristic for the stable operation of the traditional power system with SGs.

For the DC capacitor of the VSC, the power balance relationship is similar to the SG, as shown in Fig. 3(b) and (12).

$$C_{dc}\frac{\mathrm{d}V_{dc}}{\mathrm{d}t} = I_s - I_e = \frac{P_s}{V_{dc}} - \frac{P_e}{V_{dc}} \tag{12}$$

where I_s and I_e are the DC currents injected into and output from the DC capacitor, respectively.

In terms of form, the DC capacitor of the VSC can be paired with the rotor of the SG. The DC capacitance C_{dc} is comparable to the rotor inertia constant of the SG J. The DC capacitance voltage V_{dc} is comparable to the rotating speed of the SG ω_{SG}. The capacitance value maintains constant normally, and the energy stored in the DC capacitor is used to provide inertial support similar to the SGs. The VSC can provide the frequency support by simulating SGs based on the analogy, as shown in (13).

$$\delta = G_\delta(s)V_{dc0}\left(V_{dc0} - V_{dcref}\right) \tag{13}$$

where $G_\delta(s)$ is the transfer function of the V_{dc} and the power angle of the VSC δ; and V_{dc0} is the initial DC-link voltage.

The power transfer and grid synchronization are unified for the SG, as shown in Fig. 3(c). However, the power transfer and grid synchronization of the VSC are separated, as shown in Fig. 3(d). The narrow grid synchronization of the VSC is just the synchronization based on the PLL. However, the generalized synchronization of the VSC is the inner potential of the VSC (i.e., the voltage output by PWM) synchronizing with the grid, which is constituted by the power angle θ_{dc} produced by the DC voltage regulation control and the phase angle of the PLL θ_{pll}. Based on the generalized synchronization, the VSC can combine active power regulation and grid synchronization to reduce the interaction between multi-control loops by utilizing the dynamics of the capacitor.

B. Dynamic Process of DC Voltage and Energy Transfer

In this subsection, we discuss the process of energy transfer and its effect on the DC voltage, and provide a theoretical basis for the construction of synchronization control.

In the stable case, P_s and P_e are equal and the energy of the storage system is constant.

$$e = \int_0^\infty \left(P_s(t) - P_e(t)\right)\mathrm{d}t \tag{14}$$

where e is the energy in the storage medium.

We assume the DC bus voltage directly reflects the energy state of the energy storage system, as shown in (15).

$$e = \frac{1}{2}C_{dc}V_{dc}^2 \tag{15}$$

The electromagnetic power of the VSC is calculated as:

$$\frac{1}{2}C_{dc}\frac{\mathrm{d}\left(V_{dc}^2\right)}{\mathrm{d}t} = P_s - \frac{E_{VSC}U_g}{X_c + X_g}\sin\delta \tag{16}$$

where E_{VSC} is the inner potential of the VSC; and X_g is the impedance of the transmission line.

As shown in (16), we consider δ and V_{dc}^2 to be integrally related, thus δ can be regulated by adjusting the DC voltage, changing the output active power of the VSC to reach the power transfer balance. The regulation process of the control strategy is divided into three stages.

Stage 1: the output power of VSC P_e suddenly increases, and P_s and P_e become unequal, causing the DC voltage to decrease and the DC capacitor to discharge energy. Then, the control strategy reduces the power angle by changing the DC voltage, as shown in Fig. 4(a), where δ_1 is the power angle at the beginning of the disturbance; δ_2 is the power angle when P_e is equal to P_s; and ΔP_e is the power changes of

the instantaneous active power.

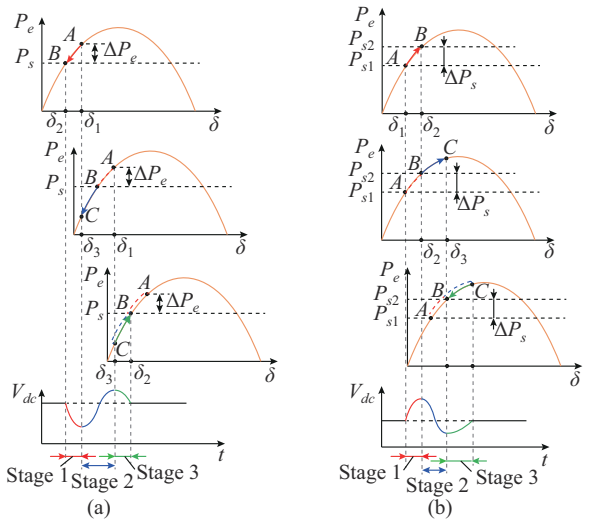

Fig. 4. Schematic diagram of dynamic process of power flow and DC voltage under disturbance. (a) Dynamic process under disturbance in output power P_e. (b) Dynamic process under disturbance in injected power P_s.

The injected power of the VSC P_s suddenly increases, and P_s and P_e become unequal, causing the DC voltage to increase and the DC capacitor to absorb energy. Then, the control strategy increases the power angle by the changes of the DC voltage, as shown in Fig. 4(b), where P_{s1} and P_{s2} are the active power of the power source before and after the disturbance, respectively; and ΔP_s is the active power changes of the power source.

Stage 2: the control strategy still works due to the decrease of the DC voltage, the power angle and P_e keep reducing, and the DC voltage begins to increase. δ_3 is the power angle during the rotor swings. For the disturbance in P_s, the control strategy still works due to the increase of the DC voltage, the power angle and P_e keep increasing, and the DC voltage begins to increase.

Stage 3: for the disturbance in P_e, the control strategy increases the power angle by the changes of the DC voltage, and P_e increases until P_s and P_e become equal. For the disturbance in P_s, the control strategy decreases the power angle by changing the DC voltage, and P_e decreases until P_s and P_e become equal. Finally, the DC voltage recovers to the initial value.

C. Proposed Strategy Based on DC-link Voltage Dynamics

The control diagram of the proposed strategy is shown in Fig. 5. The traditional PLL is not used in the normal operation of the proposed strategy. The proposed strategy can avoid the instability caused by the interaction of multiple control loops in weak grid.

1) DC Voltage Synchronization Control

Based on the mechanism analysis proposed in Section II-A, the DC-link voltage of the VSC is compared with the rotating speed of the SG. Then, the power angle of the inner potential of the VSC is directly obtained according to the square of the DC-link voltage, as shown in (17).

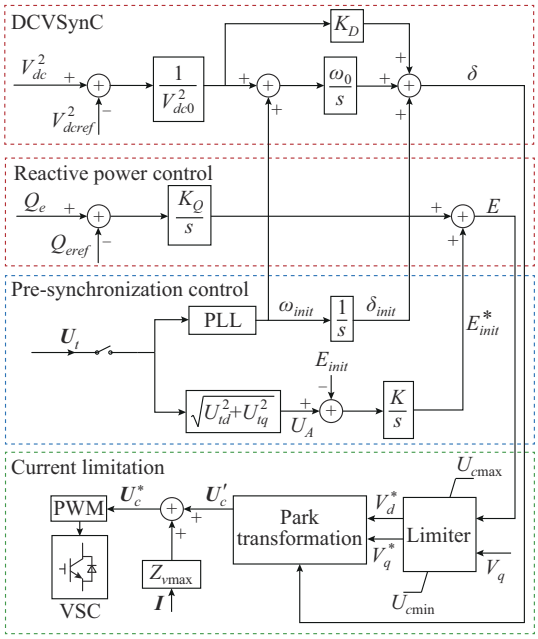

Fig. 5. Control diagram of proposed strategy.

$$\delta = \underbrace{\frac{V_{dc}^2 - V_{dcref}^2}{V_{dc0}^2}\frac{\omega_0}{s}}_{\text{Synchronization branch}} + \underbrace{\frac{V_{dc}^2 - V_{dcref}^2}{V_{dc0}^2}K_D}_{\text{Damping branch}} \tag{17}$$

where K_D is the damping coefficient of the active power control in the proposed control strategy.

2) Reactive Power Control

The reactive power control is used to control the reactive power of the VSC via directly regulating the magnitude of the inner potential of the VSC. The cascaded control is not used in the reactive power control. In the proposed strategy, the reactive power control is designed based on the integral as:

$$E = \left(Q_{eref} - Q_e\right)\frac{K_Q}{s} \tag{18}$$

where E is the magnitude of the inner potential of the VSC; and K_Q is the reactive power control parameter of the VSC.

3) Pre-synchronization Control

Before connecting with the grid, both the active power and reactive power of the VSC are zero and the corresponding controls are ineffective in synchronizing the inner potential with the grid. The pre-synchronization control is employed to synchronize the inner potential of the VSC with the grid for soft-starting. In the pre-synchronization control, the initial values of the magnitude, phase, and frequency of the inner potential of the VSC are obtained to avoid the surge during the launch of the VSC.

In the pre-synchronization control, the initial magnitude of the inner potential of the VSC is obtained by integrating the grid voltage amplitude as:

$$E_{init}^* = \left(U_m - E_{init}\right)\frac{K}{s} \tag{19}$$

where E_{init} and E_{init}^* are the magnitude of the inner potential of the VSC and its initial value, respectively; U_m is the magnitude of the terminal voltage of the VSC; and K is the volt-

age control parameter of the pre-synchronization.

In the pre-synchronization control, the initial frequency and phase of the inner potential are obtained by an additional PLL as:

$$\begin{cases} \omega_{init} = K_{ppll} U_{tq} + K_{ipll} \int U_{tq} \mathrm{d}t \\ \delta_{init} = \omega_0 \int \omega_{init} \mathrm{d}t \end{cases} \tag{20}$$

where ω_{init} is the angular frequency output by PLL; and δ_{init} is the initial value of the power angle of the VSC. After starting, the input signal $\boldsymbol{U}_t$ is disabled and the additional PLL is frozen. Then, ω_{init}, δ_{pll}, and E^*_{init} remain constant.

4) Current Limitation

The proposed strategy can not suppress the fault current in the case of a circuit fault due to the lack of current loop control. The virtual resistance and voltage phasor limitation are combined to reduce the fault current of the VSC with the proposed strategy in this paper. However, the above measures are mainly used to limit the fault current on the AC side. The chopper on the DC side is also affected by the system fault, and the DC voltage drops, which affects the synchronization process.

Under normal operation of the VSC, the virtual resistor does not work. When a system fault occurs and the current of the VSC achieves a high level, the virtual resistor is activated to reduce the fault current of the VSC by multiplying it with the current and superimposing the product onto the reference voltage.

$$\boldsymbol{U}_c^* = \boldsymbol{U}_c' + \boldsymbol{I} Z_{v\max} \tag{21}$$

$$Z_v = \begin{cases} 0 & |\boldsymbol{I}| < I_{th} \\ Z_{v\max} & |\boldsymbol{I}| \geq I_{th} \end{cases} \tag{22}$$

where Z_v is the virtual impedance; $Z_{v\max}$ is the maximum virtual impedance that can be determined considering the level of the accepted fault current; $\boldsymbol{U}_c^*$ and $\boldsymbol{U}_c'$ are the reference equivalent potential vector of the VSC and the equivalent potential vector without limitation, respectively; and I_{th} is the current threshold that triggers the virtual impedance.

The voltage phasor limiter is used to reduce the fault current of the VSC via controlling the difference between the inner potential of the VSC and the inner potential of the grid under the *dq*-axis reference frame. The *d*-axis coincides with the magnitude of the inner potential of the VSC E, and V_q= 0. The limiter is shown in Fig. 5, whose outputs V_d^* and V_q^* are the original *dq*-axis components of the output voltage reference of the VSC.

The inner potential of the VSC is confined in the safety zone.

$$\begin{cases} U_{cd\max} = U_{td} + \omega_{VSC} X_c I_{q\max} \\ U_{cd\min} = U_{td} - \omega_{VSC} X_c I_{q\max} \\ U_{cq\max} = U_{tq} + \omega_{VSC} X_c I_{d\max} \\ U_{cq\min} = U_{tq} - \omega_{VSC} X_c I_{d\max} \end{cases} \tag{23}$$

where $U_{cd\max}$ and $U_{cq\max}$ are the *d*-axis and *q*-axis components of the maximum potential of the VSC $U_{c\max}$; $U_{cd\min}$ and $U_{cq\min}$ are the *d*-axis and *q*-axis components of the minimum potential of the VSC $U_{c\min}$; $I_{d\max}$ and $I_{q\max}$ are the *d*-axis and *q*-axis components of the maximum permissible current of the VSC, respectively; and ω_{VSC} is the angular frequency of the VSC. The relationship of $I_{d\max}$ and $I_{q\max}$ is as follows:

$$\begin{cases} -I_{d\max} \leq I_d \leq I_{d\max} \\ -I_{q\max} \leq I_q \leq I_{q\max} \\ \sqrt{I_{d\max}^2 + I_{q\max}^2} \leq I_{\max} \end{cases} \tag{24}$$

where $I_{\max}$ is the maximum permissible current of the VSC.

IV. Control Design and Stability Analysis in Weak Grid

The control design and stability analysis are discussed in this section based on the small-signal models and linearized analysis method, and the model of the VSC connected with the grid is established, as shown in Fig. 6.

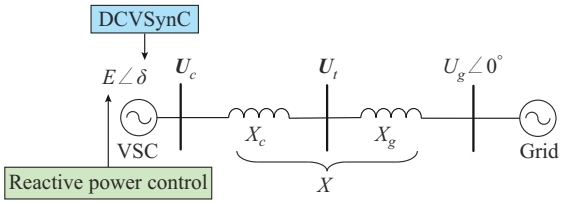

Fig. 6. Small-signal system for control design and stability analysis of proposed strategy.

A. Small-signal Model

The linearized model of the controller based on the proposed strategy is deduced by (3), (17), and (18).

$$\begin{bmatrix} \Delta\delta \\ \Delta E \end{bmatrix} = \begin{bmatrix} G_P(s) & 0 \\ 0 & G_Q(s) \end{bmatrix} \begin{bmatrix} \Delta P_s - \Delta P_e \\ \Delta Q_{eref} - \Delta Q_e \end{bmatrix} \tag{25}$$

where $G_P(s) = \dfrac{2\omega_0}{C_{dc}s^2} + \dfrac{2K_D}{C_{dc}s}$; and $G_Q(s) = \dfrac{K_Q}{s}$.

The output active power and reactive power of the VSC are injected into the point of common coupling (PCC) as:

$$\begin{cases} P_e = \dfrac{EU_g}{X} \sin\delta \\ Q_e = \dfrac{E^2}{X} - \dfrac{EU_g \cos\delta}{X} \end{cases} \tag{26}$$

where X is the impedance of the transmission line and the filter.

The linearized model of the network based on the output power of the VSC is deduced by (26).

$$\begin{bmatrix} \Delta P_e \\ \Delta Q_e \end{bmatrix} = \begin{bmatrix} G_{P\delta} & G_{PE} \\ G_{Q\delta} & G_{QE} \end{bmatrix} \begin{bmatrix} \Delta\delta \\ \Delta E \end{bmatrix} \tag{27}$$

where $G_{QE} = \dfrac{2E_0 - U_{g0}\cos\delta_0}{X}$; $G_{P\delta} = \dfrac{E_0 U_{g0}}{X}\cos\delta_0$; $G_{PE} = \dfrac{U_{g0}}{X}\sin\delta_0$; $G_{Q\delta} = \dfrac{E_0 U_{g0}}{X}\sin\delta_0$; and the subscript 0 represents the initial value.

Combine the controller (25) and the network (27) to obtain the linearized closed-loop system of the power transmission, as shown in Fig. 7.

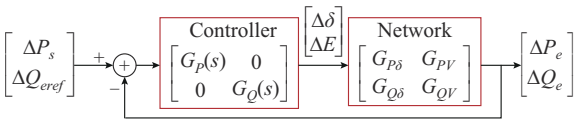

Fig. 7. Linearized small-signal model of closed-loop system.

B. Control Design

In this subsection, the impact of the main parameters on the dynamic response of the VSC is analyzed by the frequency-domain Bode diagram of the closed-loop transfer function of the VSC and the corresponding time-domain simulations, as shown in Fig. 8 and Fig. 9.

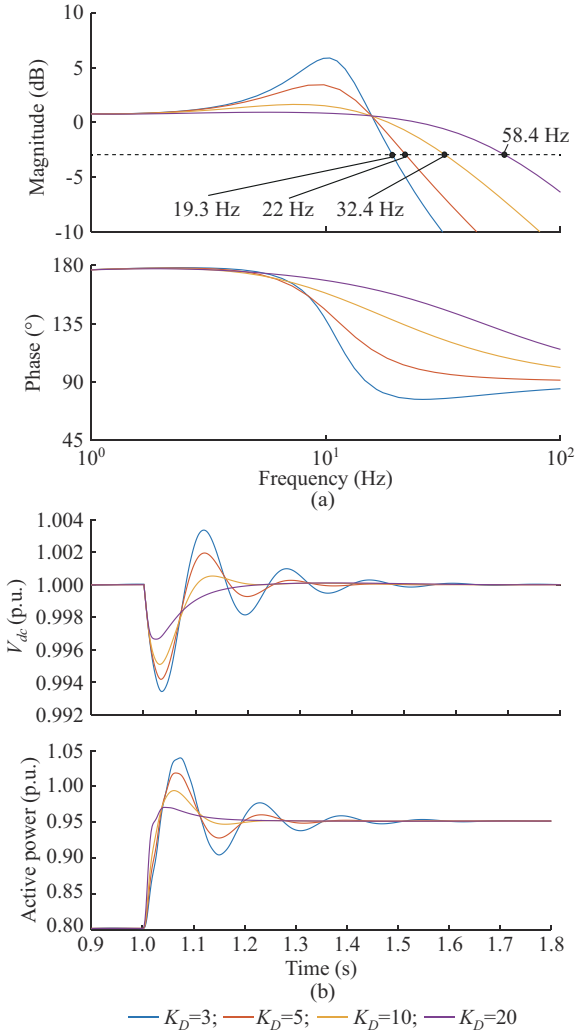

Fig. 8. Frequency-domain Bode diagram of closed-loop transfer function of VSC and time-domain simulation results with different K_D. (a) Frequency-domain Bode diagram. (b) Time-domain simulation results.

As observed from Fig. 8(a), with the increase of K_D from 3 to 20, the close-loop control bandwidth of the proposed strategy in the VSC increases from 19.3 Hz to 58.4 Hz. The higher the close-loop control bandwidth, the faster the dynamic response. Therefore, the dynamic response of the active power of the VSC is faster with the increase of the close-loop control bandwidth, as shown in Fig. 8(b), and the fluctuation of the DC-link voltage is reduced. Moreover, the corresponding time-domain simulation results illustrate that the damping ratio of the active power control of the VSC is enhanced with the increase of K_D. With the increase of K_D, the oscillations of the active power and DC-link voltage are suppressed more significantly.

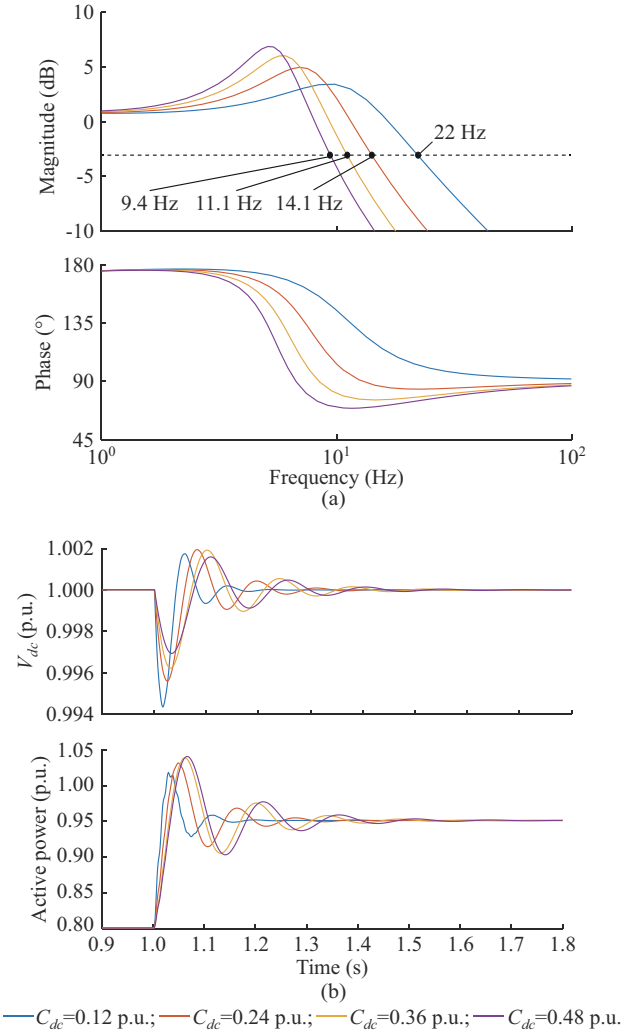

Fig. 9. Frequency-domain Bode diagram of closed-loop transfer function of VSC and time-domain simulation results with different C_{dc}. (a) Frequency-domain Bode diagram. (b) Time-domain simulation results.

As observed from Fig. 9(a), with the increase of C_{dc} from 0.12 p.u. to 0.48 p.u., the close-loop control bandwidth of the proposed strategy in the VSC decreases from 22 Hz to 9.4 Hz, while the dynamic response of the active power of the VSC is slow down, as shown Fig. 9(b). With the increase of C_{dc}, the fluctuation of the DC-link voltage is obviously reduced under disturbance. But the damping ratio is weakened and the frequency of oscillation is increased as observed from Fig. 9(b).

C. Stability Analysis

The small-signal stability of the VSC based on the proposed strategy is analyzed by the locus root of eigenvalues. The complex eigenvalues characterize the dynamics of the system, with the imaginary part indicating the oscillation characteristics and the real part indicating the damping ratio.

Combining (25) and (27), we can obtain (28), and the detailed derivation process is presented in Appendix A.

$$\frac{\Delta P_e}{\Delta P_s}=\frac{G_{P\delta}G_{\delta}(s)+G_{P\delta}G_P(s)G_{QE}G_Q(s)-}{1+G_{QE}+G_{P\delta}G_{\delta}(s)+G_{P\delta}G_P(s)G_{QE}G_Q(s)-}\rightarrow \leftarrow\frac{G_{PE}G_Q(s)G_{Q\delta}G_P(s)}{G_{PE}G_Q(s)G_{Q\delta}G_P(s)} \tag{28}$$

With the decrease of the SCR from 3 to 1.2, as shown by the arrow direction in Fig. 10, i.e., the grid is weakened, the locus root of eigenvalues of the VSC based on the traditional and proposed strategies are presented in Fig. 10(a) and (b), respectively.

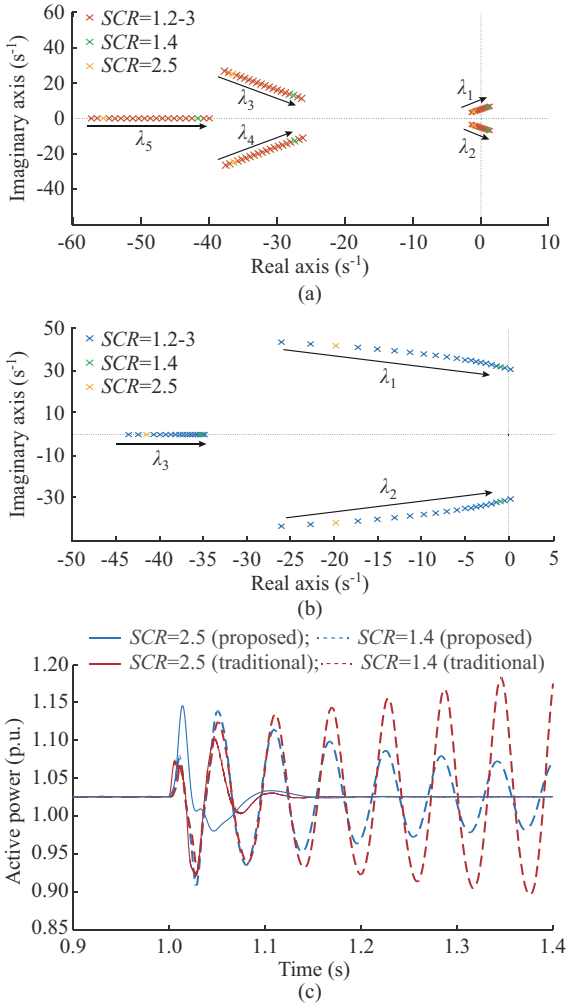

Fig. 10. Locus root of eigenvalues and corresponding time-domain simulation results of VSC with different SCRs. (a) Locus root of eigenvalues based on traditional strategy. (b) Locus root of eigenvalues based on proposed strategy. (c) Time-domain simulation results.

When $SCR=2.5$, all the eigenvalues of the traditional and proposed strategies are located at the left half plane. The details of the main eigenvalues are presented in Table I. Both the traditional and proposed strategies are able to work steadily as shown by the solid line in Fig. 10(c). With the decrease of the SCR, all the eigenvalues move towards the right half plane. When $SCR=1.4$, the eigenvalues ($\lambda_{1,2}$) of the traditional strategy are located in the right half plane, whereas all the eigenvalues of the proposed strategy are still located in the left half plane. As presented by the dashed line in Fig. 10(c), when $SCR=1.4$, the VSC based on the traditional strategy works in the state of instability and the output power shows obvious oscillatory divergence. However, the VSC based on the proposed strategy works stably, and the output power shows oscillatory convergence. It is concluded that the proposed strategy is more stable than the traditional strategy in the weak grid with a low SCR.

TABLE I
MAIN EIGENVALUES OF VSC BASED ON TRADITIONAL AND PROPOSED STRATEGIES

Strategy	Eigenvalue	$SCR=2.5$	$SCR=1.4$
Traditional	$\lambda_{1,2}$	$-1.68\pm i3.27$	$1.37\pm i5.72$
	$\lambda_{3,4}$	$-36.24\pm i23.58$	$-27.85\pm i14.64$
	λ_5	-56.2	-42.13
Proposed	$\lambda_{1,2}$	$-19.83\pm i43.56$	$-1.63\pm i32.42$
	λ_3	-42.76	-35.16

V. SIMULATION VALIDATION AND DISCUSSION

A. Simulation System Setup

A simulation system is established by MATLAB/Simulink to study the dynamic performance of the proposed strategy. In the simulation system, there are two SGs connected to Buses 1, 5 and a VSC connected to Bus 8, as shown in Fig. 11.

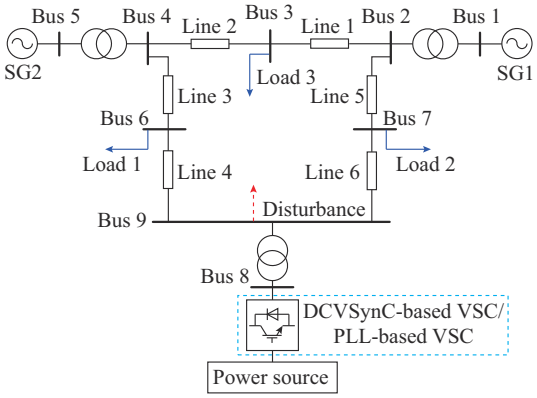

Fig. 11. Topology of small-scale power system for simulation studies.

Moreover, there are three loads connected to Buses 3, 6, and 7, respectively. The SCR at the connected point of the VSC is about 2. Based on the simulation system, the dynamic support capability of the frequency and voltage is studied. The disturbance occurs at Bus 9 by switching on and off of a load. The detailed parameters of the simulation system are presented in Appendix B. The proposed and traditional strategies are comparatively studied. A power source is connected to the DC-link of the VSC, and the output static active power reference of the VSC is set to be 0.8 p.u..

In the simulation, the primary frequency regulation is only equipped in the SGs (SG 1 and SG 2) as:

$$\Delta P_{\mathrm{mSG}i}=-R_{\mathrm{G}i}G_{\mathrm{m}i}(s)\Delta\omega_{\mathrm{SG}i}\quad i=1,2 \tag{29}$$

where $R_{\mathrm{G}i}$ is the control gain of the primary frequency regu-

lation for the i^{th} SG; ΔP_{mSGi} is the active power deviation induced by the primary frequency regulation; $G_{mi}(s)$ is the simplified transfer function of prime movers; and $\Delta\omega_{SGi}$ is the rotating speed change of the i^{th} SG. For the thermal power generator, the transfer function of the prime mover can be expressed as:

$$G_{mi}(s)=\frac{1+F_{HP}T_{RH}s}{(1+T_{CH}s)(1+T_{RH}s)} \tag{30}$$

where F_{HP}, T_{RH}, and T_{CH} are the parameters of the prime mover.

The voltage is regulated by the Q-V droop control equipped in the VSC, which produces the reactive power reference for the VSC as:

$$Q_{eref}=K_{\Delta V}(U_m-U_{mref})\frac{1}{1+sT_m} \tag{31}$$

where U_m and U_{mref} are the measured and reference values of the terminal voltage of the VSC, respectively; $K_{\Delta V}$ is the control coefficient of the voltage regulation control; and T_m is the time constant of the detection unit. The simplified detection unit is used to measure the terminal voltage of the VSC.

B. Dynamic Frequency Support Capability

When the active power of the load is increased by 0.1 p.u. at 5 s, the dynamic responses of the system with the traditional PLL and proposed strategies are shown in Fig. 12.

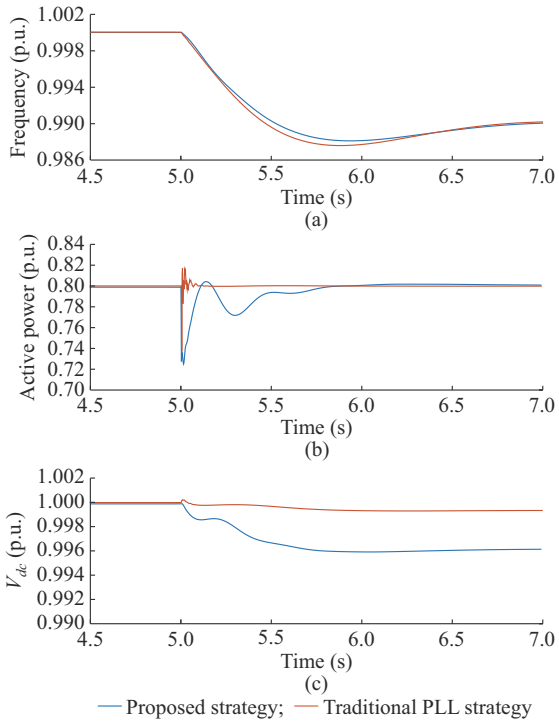

Fig. 12. Dynamic responses of grid frequency and active power and DC-link voltage of VSC with traditional PLL and proposed strategies under active power disturbance in grid. (a) Grid frequency. (b) Active power. (c) DC-link voltage.

The rate of change of the frequency (ROCOF) is reduced and the nadir of grid frequency is increased with the proposed strategy, as shown in Fig. 12(a). Under disturbance, the proposed strategy is able to naturally provide active power to support grid frequency with almost no time delay, but the traditional PLL strategy will not provide any active power support for the grid frequency, as shown in Fig. 12(b). Thus, the proposed strategy is positive to improve the grid frequency dynamics. Moreover, after disturbance, the grid frequency (i.e., the rotating speed of the SG) is changed to 0.99 p.u.. With the change of grid frequency, the DC-link voltage with the traditional PLL strategy is the same as before the disturbance. However, after disturbance, the DC-link voltage with the proposed strategy is the deviation from the steady-state value before the disturbance, as shown in Fig. 12(c), due to that it is in analogy with the rotating speed of the SG, which will change with grid frequency deviations.

The impact of the proposed strategy on the grid frequency and the active power and DC-link voltage of the VSC with the increase of the DC capacitor (C_{dc}) from 0.24 p.u. to 0.48 p.u. is analyzed, and the simulation results are shown in Fig. 13. With the increase of C_{dc}, the equivalent inertia is increased. The ROCOF is reduced and the nadir of the grid frequency is increased with the increase of C_{dc}, as shown in Fig. 13(a). Moreover, the proposed strategy provides more dynamic support of the active power during a longer time period with the increase of C_{dc}, as shown in Fig. 13(b). The decline rate of the DC-link voltage (V_{dc}) is gradually reduced with larger C_{dc}, as shown in Fig. 13(c).

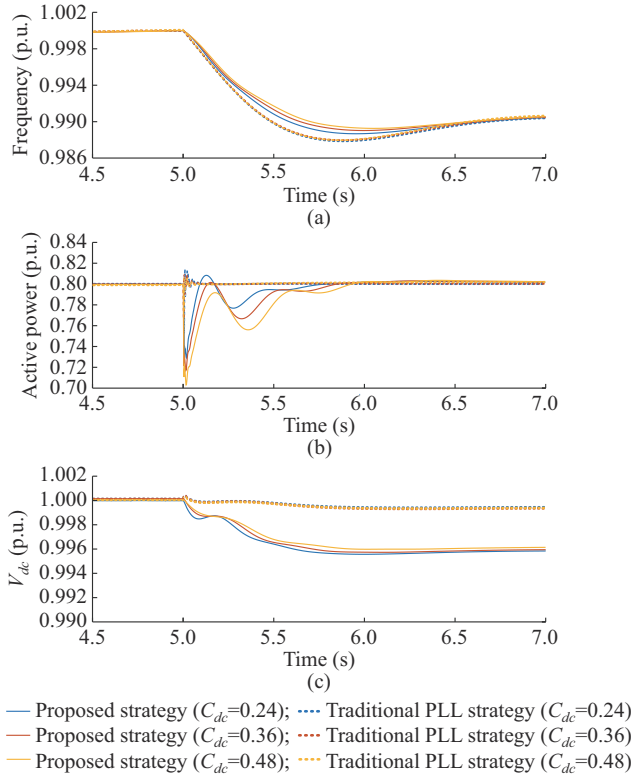

Fig. 13. Dynamic responses of grid frequency and active power and DC-link voltage of VSC with proposed and traditional strategies under different C_{dc}. (a) Grid frequency. (b) Active power. (c) DC-link voltage.

C. Dynamic Voltage Support Capability

When the reactive power of the load is increased by 0.1 p.u. at 5 s, the dynamic responses of the reactive power of the VSC and the grid voltage with the traditional Q-V droop and proposed strategies are shown in Fig. 14. In the simulation,

the voltage control is set with the same structure and parameters. Thus, the steady-state reactive power of both control strategies is the same, as shown in Fig. 14(a). However, the maximum voltage deviation is reduced and the dynamic performance of grid voltage with the proposed strategy is better than that with the traditional *Q-V* droop strategy, as shown in Fig. 14(b). Because the proposed strategy is equivalent to a voltage source and is able to spontaneously provide dynamic reactive power support for the grid prior to the functioning of the voltage control, as shown in Fig. 14(a), the dynamic voltage support capability of the proposed strategy is better than that of the traditional *Q-V* droop strategy.

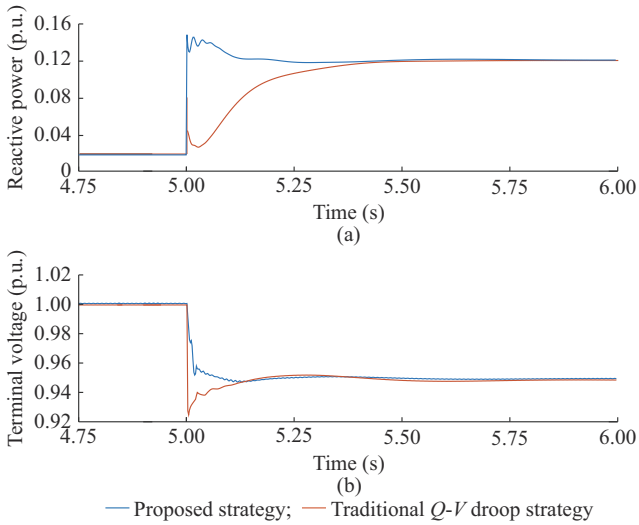

Fig. 14. Dynamic responses of reactive power of VSC and grid voltage with traditional *Q-V* droop and proposed strategies under reactive power disturbance. (a) Reactive power. (b) Grid voltage.

The impact of the proposed strategy on the reactive power of the VSC and the grid voltage with the increase of K_Q from 0.8 to 1.5 is analyzed, and the simulation results are presented in Fig. 15. With the increase of K_Q, the reactive power from the proposed strategy is decreased, as shown in Fig. 15(a). Moreover, the voltage deviation is increased with the increase of K_Q, as shown in Fig. 15(b). Thus, the dynamic voltage support capability of the proposed strategy is weakened with the increase of K_Q.

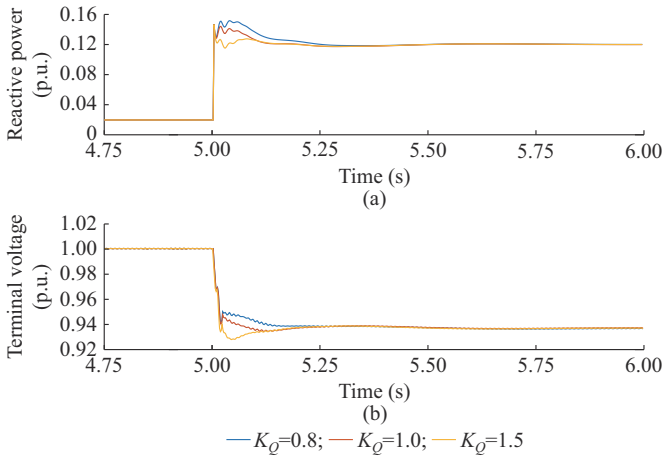

Fig. 15. Dynamic responses of reactive power of VSC and grid voltage with proposed strategy under different K_Q. (a) Reactive power. (b) Grid voltage.

VI. Conclusion

This paper presents a control strategy for grid-connected VSC with the functions of the grid synchronization and power regulation. The mechanism, control design, stability analysis, and dynamic support capability of the proposed strategy are analyzed. Moreover, simulations are implemented to validate the correctness and effectiveness of the proposed strategy on the dynamic support capability of the grid frequency and voltage as well as stability enhancement in weak grids. Some conclusions are drawn as follows.

1) The proposed strategy can improve the stability by combining the synchronization with the grid and the active power regulation of the VSC according to the dynamic of the DC capacitor.

2) The proposed strategy can enhance the dynamic support capability of the grid frequency and voltage by removing the PLL and inner-current loop to avoid the interaction between them.

3) The proposed strategy makes the inner potential have the inertia characteristic and have a natural response to grid frequency and voltage dynamics.

Appendix A

The derivation process of the small-signal model is as follows.

Substitute (25) into (27) to eliminate intermediate variables ΔE and $\Delta\delta$. Make $\Delta Q_{eref}=0$, and we can obtain:

$$\begin{cases}\Delta P_e = G_{P\delta}G_P(s)\left(\Delta P_s-\Delta P_e\right)-G_{PE}G_Q(s)\Delta Q_e\\ \Delta Q_e = G_{Q\delta}G_P(s)\left(\Delta P_s-\Delta P_e\right)-G_{QE}G_Q(s)\Delta Q_e\end{cases} \tag{A1}$$

The reactive power can be calculated by transforming the reactive power formula in (A1).

$$\Delta Q_e = \frac{G_{Q\delta}G_P(s)\left(\Delta P_s-\Delta P_e\right)}{1+G_{QE}G_Q(s)} \tag{A2}$$

The active power can be calculated by substituting (A2) into (A1).

$$\Delta P_e = G_{P\delta}G_P(s)\left(\Delta P_s-\Delta P_e\right)-G_{PE}G_Q(s)\frac{G_{Q\delta}G_P(s)\left(\Delta P_s-\Delta P_e\right)}{1+G_{QE}G_Q(s)} \tag{A3}$$

The transfer function of single input and single output of active power (28) can be obtained by modifying (A3).

Appendix B

The detailed parameters of the simulation system in Fig. 11 are as follows.

1) Parameters of the main circuit of the VSC: the base value of power S_B is 100 MVA; the frequency f_B is 50 Hz; the phase to phase voltage V_B is 0.96 kV; the DC-link capital voltage $V_{B\text{-}dc}$ is 1.2 kV; the impedance of the transmission line X_g is 0.19 p.u.; the impedance of the filter X_c is 0.05 p.u.; the referred DC-link voltage V_{dcref} is 1.0 p.u.; and the capacitance of the DC-link capacitor C_{dc} is 0.12 p.u..

2) Control parameters of the proposed DCVSynC: the damping coefficient K_D is 10 and the reactive voltage control factor

K_Q is 0.5.

3) Control parameters of traditional control based on PLL: the control parameters of the AC current controller K_{pc} and K_{ic} are 3 and 20, respectively; the control parameters of the DC voltage control K_{pdc} and K_{idc} are 7 and 500, respectively; and the control parameters of the reactive power control K_{pr} and K_{ir} are 0.1 and 5, respectively.

REFERENCES

[1] X. Li, R. Ma, W. Gan *et al*., "Optimal dispatch for battery energy storage station in distribution network considering voltage distribution improvement and peak load shifting," *Journal of Modern Power Systems and Clean Energy*, vol. 10, no. 1, pp. 131-139, Jan. 2022.

[2] L. F. Ugarte, M. C. de Almeida, and L. H. T. Bandória, "Fault location approach to distribution networks based on custom state estimator," *Journal of Modern Power Systems and Clean Energy*, vol. 11, no. 6, pp. 1878-1889, Nov. 2023.

[3] Y. Yang, D. Zhu, X. Zou *et al*., "Power compensation control for DFIG-based wind turbines to enhance synchronization stability during severe grid faults," *IEEE Transactions on Power Electronics*, vol. 37, no. 9, pp. 10139-10143, Sept. 2022.

[4] X. Guo, D. Zhu, X. Zou *et al*., "Analysis and enhancement of active power transfer capability for DFIG-based WTs in very weak grid," *IEEE Journal of Emerging and Selected Topics in Power Electronics*, vol. 10, no. 4, pp. 3895-3906, Aug. 2022.

[5] N. Flourentzou, V. G. Agelidis, and G. D. Demetriades, "VSC-based HVDC power transmission systems: an overview," *IEEE Transactions on Power Electronics*, vol. 24, no. 3, pp. 592-602, Mar. 2009.

[6] B. Singh and J. Solanki, "A comparison of control algorithms for DSTATCOM," *IEEE Transactions on Industrial Electronics*, vol. 56, no. 7, pp. 2738-2745, Jul. 2009.

[7] L. Shang, X. Dong, C. Liu *et al*., "Fast grid frequency and voltage control of battery energy storage system based on the amplitude-phase-locked-loop," *IEEE Transactions on Smart Grid*, vol. 13, no. 2, pp. 941-953, Mar. 2022.

[8] D. E. Olivares, A. Mehrizi-Sani, A. H. Etemadi *et al*., "Trends in microgrid control," *IEEE Transactions on Smart Grid*, vol. 5, no. 4, pp. 1905-1919, Jul. 2014.

[9] V. Blasko and V. Kaura, "A new mathematical model and control of a three-phase AC-DC voltage source converter," *IEEE Transactions on Power Electronics*, vol. 12, no. 1, pp. 116-123, Jan. 1997.

[10] D. Chen and L. Xu, "Autonomous DC voltage control of a DC microgrid with multiple slack terminals," *IEEE Transactions on Power Systems*, vol. 27, no. 4, pp. 1897-1905, Nov. 2012.

[11] A. Musengimana, X. Zheng, and H. Li, "Improved auto-synchronisation of grid-connected PV inverter based on the DC capacitor voltage control," *IET Renewable Power Generation*, vol. 14, no. 5, pp. 684-694, Apr. 2020.

[12] M. Mehrasa, E. Pouresmaeil, A. Sepehr *et al*., "Control technique for the operation of grid-tied converters with high penetration of renewable energy resources," *Electric Power Systems Research*, vol. 166, pp. 18-28, Jan. 2019.

[13] H. Yuan, X. Yuan, and J. Hu, "Modeling of grid-connected VSCs for power system small-signal stability analysis in DC-link voltage control timescale," *IEEE Transactions on Power Systems*, vol. 32, no. 5, pp. 3981-3991, Sept. 2017.

[14] J. Rocabert, A. Luna, F. Blaabjerg *et al*., "Control of power converters in AC microgrids," *IEEE Transactions on Power Electronics*, vol. 27, no. 11, pp. 4734-4749, Nov. 2012.

[15] Ö. Göksu, R. Teodorescu, P. Rodriguez *et al*., "A review of the state of the art in control of variable-speed wind turbines," in *Proceedings of 9th International Workshop on Large-scale Integration of Wind Power into Power Systems*, Aarhus, Denmark, Oct. 2010, pp. 1-8.

[16] D. Wang, L. Liang, J. Hu *et al*., "Analysis of low-frequency stability in grid-tied DFIGs by nonminimum phase zero identification," *IEEE Transactions on Energy Conversion*, vol. 33, no. 2, pp. 716-729, Jun. 2018.

[17] J. Zhu, Z. Guo, J. Hu *et al*., "Truncation number selection of harmonic state-space model based on the Floquet characteristic exponent," *IEEE Transactions on Industrial Electronics*, vol. 70, no. 3, pp. 3222-3228, Mar. 2023.

[18] Y. Huang, X. Yuan, J. Hu *et al*., "Modeling of VSC connected to weak grid for stability analysis of DC-link voltage control," *IEEE Journal of Emerging and Selected Topics in Power Electronics*, vol. 3, no. 4, pp. 1193-1204, Dec. 2015.

[19] Y. Huang, D. Wang, L. Shang *et al*., "Modeling and stability analysis of DC-link voltage control in multi-VSCs with integrated to weak grid," *IEEE Transactions on Energy Conversion*, vol. 32, no. 3, pp. 1127-1138, Sept. 2017.

[20] L. Huang, H. Xin, Z. Li *et al*., "Grid-synchronization stability analysis and loop shaping for PLL-based power converters with different reactive power control," *IEEE Transactions on Smart Grid*, vol. 11, no. 1, pp. 501-516, Jan. 2020.

[21] D. Wang, L. Liang, L. Shi *et al*., "Analysis of modal resonance between PLL and DC-link voltage control in weak-grid tied VSCs," *IEEE Transactions on Power Systems*, vol. 34, no. 2, pp. 1127-1138, Mar. 2019.

[22] F. M. Hughes, O. Anaya-Lara, N. Jenkins *et al*., "Control of DFIG-based wind generation for power network support," *IEEE Transactions on Power Systems*, vol. 20, no. 4, pp. 1958-1966, Nov. 2005.

[23] P. Paitandy and S. Mishra, "Nonlinear disturbance observer based DC-link voltage control for grid-connected VSC," in *Proceedings of 2020 3rd International Conference on Energy, Power and Environment: Towards Clean Energy Technologies*, Shillong, India, Mar. 2021, pp. 1-5.

[24] J. M. Mauricio, A. Marano, A. Gomez-Exposito *et al*., "Frequency regulation contribution through variable-speed wind energy conversion systems," *IEEE Transactions on Power Systems*, vol. 24, no. 1, pp. 173-180, Feb. 2009.

[25] L. Shang, Z. Hua, C. Liu *et al*., "Amplitude-phase-locked-loop-based power injection strategy for wind power generation under three-phase grid fault," *IEEE Transactions on Energy Conversion*, vol. 37, no. 4, pp. 2952-2961, Dec. 2022.

[26] J. F. Conroy and R. Watson, "Frequency response capability of full converter wind turbine generators in comparison to conventional generation," *IEEE Transactions on Power Systems*, vol. 23, no. 2, pp. 649-656, May 2008.

[27] L. Shang, C. Han, X. Dong *et al*., "Voltage source converter-based voltage stiffness compensator to improve grid voltage dynamics," *Frontiers in Energy Research*, vol. 10, p. 835066, Feb. 2022.

[28] Y. Zuo, G. Frigo, A. Derviškadić *et al*., "Impact of synchrophasor estimation algorithms in ROCOF-based under-frequency load-shedding," *IEEE Transactions on Power Systems*, vol. 35, no. 2, pp. 1305-1316, Mar. 2020.

[29] Q. Zhong and G. Weiss, "Synchronverters: inverters that mimic synchronous generators," *IEEE Transactions on Industrial Electronics*, vol. 58, no. 4, pp. 1259-1267, Apr. 2011.

[30] H. Bevrani, T. Ise, and Y. Miura, "Virtual synchronous generators: a survey and new perspectives," *International Journal of Electrical Power & Energy Systems*, vol. 54, pp. 244-254, Jan. 2014.

[31] S. Wang, J. Hu, and X. Yuan, "Virtual synchronous control for grid-connected DFIG-based wind turbines," *IEEE Journal of Emerging and Selected Topics in Power Electronics*, vol. 3, no. 4, pp. 932-944, Dec. 2015.

[32] L. Zhang, L. Harnefors, and H. P. Nee, "Power-synchronization control of grid-connected voltage-source converters," *IEEE Transactions on Power Systems*, vol. 25, no. 2, pp. 809-820, May 2010.

[33] S. M. Ashabani and Y. A. R I. Mohamed, "New family of microgrid control and management strategies in smart distribution grids – analysis, comparison and testing," *IEEE Transactions on Power Systems*, vol. 29, no. 5, pp. 2257-2269, Sept. 2014.

[34] M. Guan, W. Pan, J. Zhang *et al*., "Synchronous generator emulation control strategy for voltage source converter (VSC) stations," *IEEE Transactions on Power Systems*, vol. 30, no. 6, pp. 3093-3101, Nov. 2015.

[35] L. Huang, H. Xin, Z. Wang *et al*., "A virtual synchronous control for voltage-source converters utilizing dynamics of DC-link capacitor to realize self-synchronization," *IEEE Journal of Emerging and Selected Topics in Power Electronics*, vol. 5, no. 4, pp. 1565-1577, Dec. 2017.

[36] L. Huang, H. Xin, H. Yang *et al*., "Interconnecting very weak AC systems by multiterminal VSC-HVDC links with a unified virtual synchronous control," *IEEE Journal of Emerging and Selected Topics in Power Electronics*, vol. 6, no. 3, pp. 1041-1053, Sept. 2018.

[37] L. Shang, X. Dong, C. Liu *et al*., "Fast grid frequency and voltage control of battery energy storage system based on the amplitude-phase-locked-loop," *IEEE Transactions on Smart Grid*, vol. 13, no. 2, pp. 941-953, Mar. 2022.

Chunyi Han received the B.S. degree from the School of Electrical Engineering and Automation, Hefei University of Technology, Hefei, China, in

2021. She is currently pursing the M.S. degree in electrical engineering with Wuhan University, Wuhan, China. Her research interests include inverter control technology and dynamic analysis of microgrid.

Lei Shang received the B.Sc. degree in electrical engineering from the Nanjing University of Posts and Telecommunications, Nanjing, China, in 2008, the M.Eng. degree in electrical engineering from Zhejiang University, Hangzhou, Chian, in 2011, and the Ph.D. degree in electrical engineering from the Huazhong University of Science and Technology, Wuhan, China, in 2017. He is a Lecturer with the Department of Electrical Engineering and Automation, Wuhan University, Wuhan, China. He was with Nari-Relays Electric Company, Ltd., Nanjing, China, as an Engineer from 2011 to 2012, and with the Institute of New Energy, Wuhan, China, as a Project Manager from 2017 to 2020. His current research interests include dynamic analysis and control of microgrid with large-scale renewables.

Shi Su received the B.S. degree from Southeast University, Nanjing, China, and the M.S. degree from Yunnan University, Kunming, China. He is Senior Engineer at professor level, Secondary Technical Expert of Yunnan Power Grid Company, Kunming, China, and Young and Middle-aged Academic and Technical Leaders in Yunnan province. His main research interests include automation, new energy, and smart grid.

Xuzhu Dong received the M.S. and Ph.D. degrees from Tsinghua University, Beijing, China, in 1995 and 1998, respectively, and the second Ph.D. degree from Virginia Tech, Virginia, USA, in 2002. He is a Professor and the Dean of the School of Electrical Engineering and Automation, Wuhan University, Wuhan, China. He was the Deputy Chief Engineer and the Director of the Smart Grid Institute of China Southern Power Grid (CSG) Electric Power Research Institute (EPRI), Guangzhou, China. Before joined CSG, he worked with Progress Energy, FirstEnergy, and EPRI solutions in USA, as a Senior Engineer, Stuff Engineer, and Lead Engineer. He was involved into several key smart grid demonstration projects with CSG. He is a member of CIGRE. His research interests include smart distributions, microgrids, integration of renewable energy, energy storage, and asset management.

Bo Wang received the Ph.D. degree in computer science from Wuhan University, Wuhan, China, in 2006. He did a Post-doctoral Research with the School of Electrical Engineering, Wuhan University, from 2007 to 2009, where he is currently a Professor with the School of Electrical Engineering. His research interests include power system online assessment, big data, and integrated energy systems.

Hao Bai received the M.S. and Ph.D. degrees from Huazhong University of Science and Technology, Wuhan, China, in 2014 and 2016, respectively. He is currently a Senior Engineer with China Southern Power Grid Electric Power Research Institute, Guangzhou, China. His research interests include smart grid, active distribution network, and artificial intelligence.

Wei Li received the B.S. and M.S. degrees in electrical engineering from Tsinghua University, Beijing, China, in 2016 and 2018, respectively. He is currently an Engineer of power distribution with China Southern Power Grid Electric Power Research Institute, Guangzhou, China. His research interests include smart distribution systems, dispatch of distribution networks, and integration of distributed generation into electric power systems.